Energy Storage Materials 88 (2026) 105101

Contents lists available at ScienceDirect

Energy Storage Materials

journal homepage: www.elsevier.com/locate/ensm

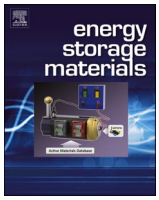

Bioacid mediated biocarbon for competitive sodium-ion battery

Xinlin Shi [a,1], Guobiao Jin [1,a], Jie Lin [1,a], Feng Jin [a,*], Rui Liu [a], Lu Wang [a], Yumeng Lan [a], Zhihao Shen [a], Qimin Tian [a], Hongzhou Lu [a], Xinjun Qian [a], Qingsong Wang [a], Keao Wu [a], Junping Jia [b], Haipeng Yang [b], Hai Lin [a], Zirui Lou [a,*], Feng Pan [a,*]

[a] School of Advanced Materials, Peking University Shenzhen Graduate School, Shenzhen, 518055, China
[b] College of Materials Science and Engineering, Shenzhen University, Shenzhen 518060, PR China

ARTICLE INFO

Keywords:
Biomass-derived hard carbon
Green deashing
Pore engineering
Sodium-ion batteries
Closed-loop recyclable

ABSTRACT

Massive production of high-performance biocarbon is essential for an electrified, green and sustainable society. However, its practical fabrication is still challenging due to stringent porosity requirements and reliance on toxic substances in the biomass deashing process. Particularly, hard carbons (HCs) suffer from unprecise pore regulation and impurity elements arising from precursors. Herein, we developed a biomass-derived HC treated with bioacid (phytic acid, PA) that enables one-step green deashing and precise pore engineering. The optimized HC anode derived from cellulose, with remarkable carbon yield (~ 40%, close to its theoretical value), exhibits a Na-storage capacity of 483 mAh g^{-1} with a high initial Coulomb efficiency (ICE) of 90%. Besides, PA showed great potential in recyclability. Furthermore, life cycle assessment (LCA) analysis reveals that the proposed process reduces fossil depletion by 50% and greenhouse gas emissions by 60%. Our work opens a new avenue to massive production for the high-performance HC based on biomass through green, sustainable paths.

1. Introduction

The global energy transition increasingly centers on scaling renewable resources, modernizing energy infrastructure, and steadily reducing reliance on fossil fuels to meet green and sustainability targets [1–2]. Electrochemical storage technologies played a critical role in the a green society since they buffer the temporal mismatch between renewable energy generation and demand, enabling stable and dispatchable power from variable sources like solar and wind.

Carbon-based materials, serving as electrodes or conductive agents in electrochemical energy storage systems,are attractive due to their high electron conductance, tunable structures, and exceptional stability [3].

Unlike conventional carbon derived from fossil fuel (eg: coal and petrochemicals), biocarbon is sustainable and eco-friendly since it originates directly or indirectly from plant photosynthesis, which acquires considerable attraction[4–6]. However, there are some significant challenges sitting in the environmental fabrication for high-performance biocarbon, including: 1) low porosity and wide pore size distribution of biocarbon derived from the direct pyrolysis of biomass result in poor electrochemical performances; [7–8] 2) comparable ash (~7.2%) derived from the biomass promotes slagging and fouling of processing equipment; and it also forms inorganic impurities to the final products[9–10]. 3) To remove it, inorganic acid leaching agents (such as HNO_3, HCl, and H_2SO_4) are used, which impose significant environmental costs [11]. 4) Hazardous gases releasing and acidic waste generated during leaching lead to serious operational safety [12].

Hard carbons (HCs), one of the most representative carbon-based materials, have been widely used as anode for sodium-ion batteries (SIBs) due to its high specific capacity (>300 mAh g^{-1}) and low-voltage plateau (<0.1 V vs Na^+/Na)[13–14]. Structurally, HC is a turbostratic carbon composed of randomly oriented, curved, and defective graphene nanosheets with enlarged interlayer spacing[15–16]. Recently, it was reported that low-voltage plateau was related to closed pores for sodium storage [17–18]. Specifically, it is effective method to increase the plateau capacity of HC through generating high density of closed pores. Komaba et al. reported HC obtained through pyrolyzing zinc gluconate delivered an ultrahigh sodium storage capacity of 480 mAh g^{-1}[19]. However, this method was restricted to specific precursors, not compatible with biomass precursors. Besides, a plateau capacity exceeding 400 mAh g^{-1} was achieved with activated carbon as precursor

* Corresponding authors.
E-mail addresses: jin.feng@pku.edu.cn (F. Jin), zrlou@pku.edu.cn (Z. Lou), panfeng@pkusz.edu.cn (F. Pan).
[1] Xinlin Shi, Guobiao Jin and Jie Lin contributed equally to this work.

https://doi.org/10.1016/j.ensm.2026.105101
Received 2 February 2026; Received in revised form 3 April 2026; Accepted 8 April 2026
Available online 9 April 2026

and through chemical vapor deposition (CVD). Small carbon species entered into the pores and controlled the pore structure precisely[20]. Nevertheless, the CVD process requires expensive equipments and complex procedures, making it impractical for large-scale or industrial applications[4–5,21]. Other emerging strategies for closed pore construction in HCs have been explored recently, such as flash heating [22–24], molecular crosslinking[25–27] and biomass decoupling[28], which exhibit promising pore regulation efficiency but still face challenges in scalable fabrication for biomass-derived precursors. Additionally, HC is highly sensitive to impurity elements, which can impair the reversible storage of sodium ions and result in low initial coulombic efficiency (ICE) or significant gas evolution[29–30]. Thus, it is urgent to develop a universal, cheap and sustainable method to process HC with high performances.

In this study, we proposed a simple one-step method for pore engineering and deashing process simultaneously for bamboo-derived HCs using phytic acid (PA) treatment and demonstrated its effectiveness as anodes for SIB (Fig. 1a). The results indicated that PA leaching can remove over 80% of ash from bamboo precursors and form uniformly pore-rich structure within the carbon matrix. During high-temperature carbonization process, these pores were *in-situ* transformed into closed pores, which resulted in enhanced sodium storage capabilities with initial specific capacity of 471 mAh g^{-1} and coulombic efficiency of 90%. And it was evident that PA concentration affected its distribution in cellulose matrix, which further determined the pore structure in HCs. Moreover, PA can be readily recycled in the whole process. The obtained HC treated with reused PA still delivered high specific capacity (416 mAh g^{-1} with PA recycled for five times), underscoring the environmental sustainability of this method. Additionally, life cycle assessment (LCA) demonstrated that the proposed process reduces fossil depletion by 50% and greenhouse gas emissions by 60%, proving its enhanced environmental friendliness and sustainability. Our work exhibits a new, cost-effective, recyclable and sustainable method for bamboo-derived HCs with high performances (Fig. 1b), which provides the guidance for the rational design of green and sustainable biocarbon fabrications.

2. Results and discussions

2.1. PA one-step biomass deashing and pore engineering

Bamboo, a member of the subfamily Bambusoideae of the grass family (Poaceae), is one of the fastest-growing plants in the world,

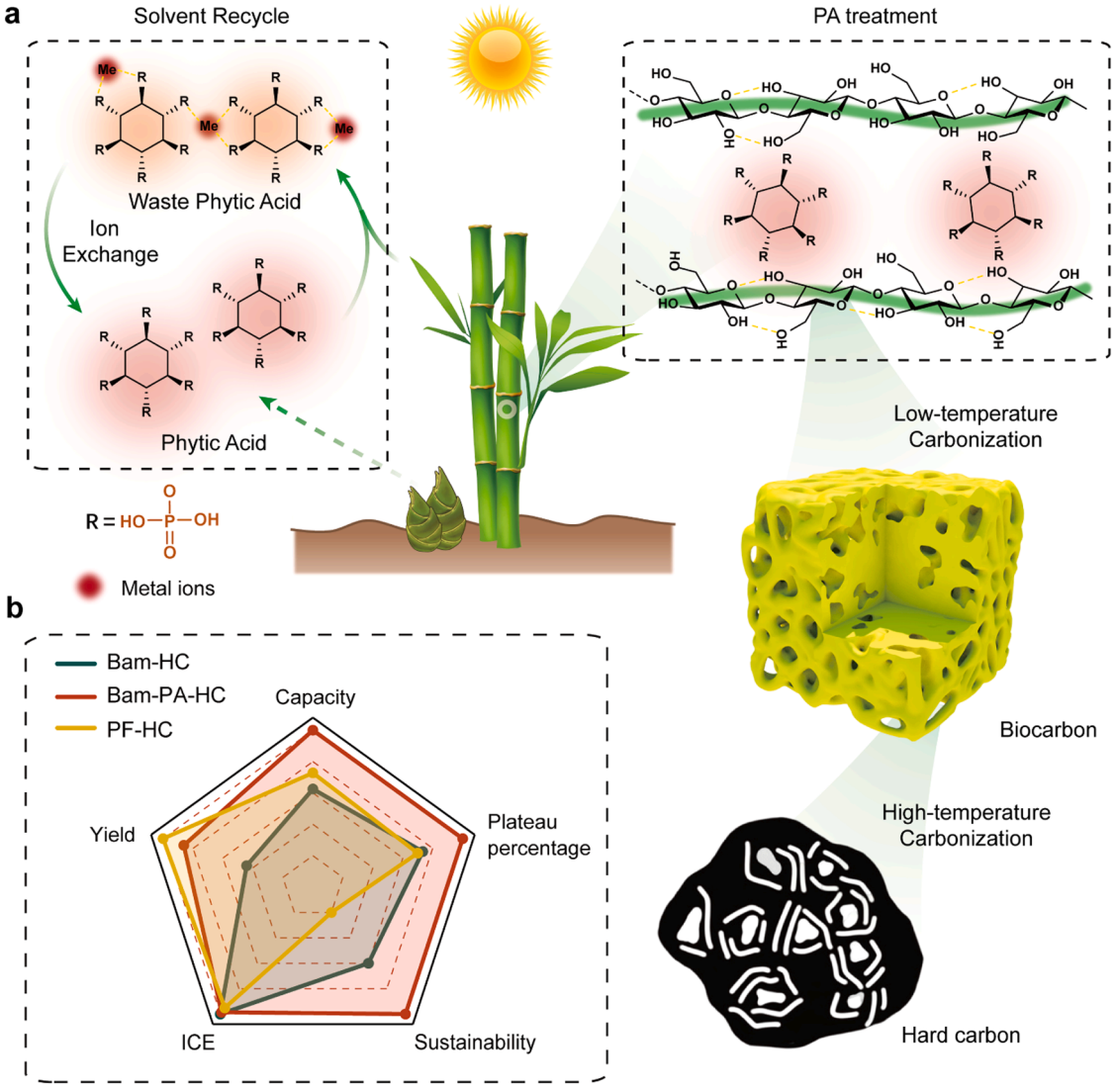

Fig. 1. . Fabrication mechanism and advantages of this method.
a, Schematic of the synthesis of PA mediated bamboo-based HC (Bam-PA-HC). b, Radar chart illustrating the advantages of Bam-PA-HC. (Traditional bamboo-based HC, Bam-HC; Phenol formaldehyde resin-based HC, PF-HC) The scoring criteria for the scale are elaborated in Methods.

serving it as a highly competitive precursor for biomass-derived carbon materials. And PA, or inositol hexa-phosphate, a natural and non-toxic compound, widely exists in plant seeds and embryos and is extensively used in the food and cosmetics industries. Structurally, the PA molecule contains six phosphate groups, conferring a strong chelating ability, which enables it to form stable complexes with various metal ions (e.g., Zn^{2+}, Cu^{2+}, Fe^{2+}, Mg^{2+}, Ca^{2+}). Here, HCs were obtained from bamboo through recyclable PA as deashing agent and subsequent two-step carbonization process (Fig. 2a).

To evaluate the effect of PA as deashing agent, ICP-OES tests were conducted. And the results showed that the removal efficiency of K, Ca, Mg, Fe, Mn, and Zn exceeded 90% (Supplementary Fig. 1 and Fig. 2b), and ash content analysis also showed >80% of the ash in bamboo powder was removed (Supplementary Figs. 2 and 3). Furthermore, most K and Zn are volatilized after carbonization process at 1600 °C, whereas other elements, including, Ca, Fe, Mn, and Mg, were still enriched in the obtained HC. In Bam-1600, multiple metal elements showed high concentrations (for example: Fe: 561 mg/kg). In contrast, these metal elements were almost undetectable in Bam-PA-1600 (Fig. 2c). And Fe exhibited extremely low signal (< 5 mg/kg), much lower than the limitation (100 mg/kg) in Chinese National Standard (GB/T 43114-2023). Moreover, the treated bamboo powder showed an unprecedented increase in carbon yield (from 19.91% to 38.77%), surpassing most reported bio-based HC and many resin-based HC (Fig. 2d and Supplementary Table 1).

Furthermore, to evident the functionality of PA as pore former, structures of carbon samples were investigated, including N_2 adsorption-desorption measurements, Small-angle X-ray scattering (SAXS), Transmission Electron Microscopy (TEM), Raman Spectroscopy and X-ray diffraction (XRD).

Based on BET model, Bam-PA-400 showed high specific surface area (SSA) (1063.32 m^2/g), proving functionality of PA as pore former. After carbonization at 1600 °C, the SSA decreased dramatically to 138.93 m^2/g, which originated from conversion open pores to close pores (Supplementary Fig. 4). SAXS patterns showed increased scattering intensities at 0.1–0.2 $Å^{-1}$ for Bam-PA-1600 and the obtained refined results

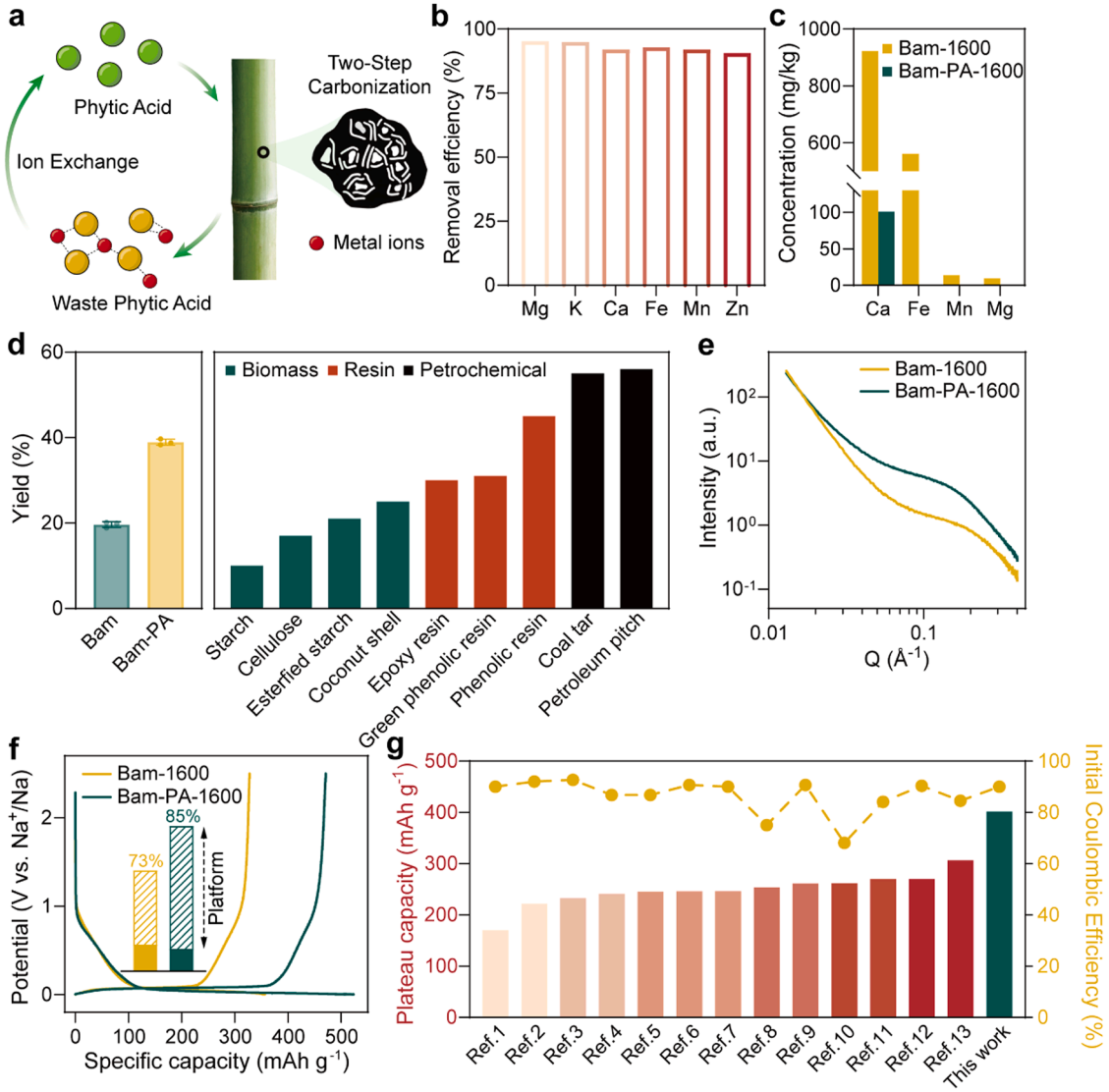

Fig. 2. . Characterization of deashing and pore engineering.
a, Schematic of the synthesis process for Bam-PA-HC; b, Metal elements removal efficiency of bamboo powder; c, The content of metal elements collected from ICP-OES for Bam-HC and Bam-PA-HC; d, Carbon yield of Bam, Bam-PA and other precursors (from precursors to HC) [15,31–34]; e, Small-angle X-ray scattering patterns; f, Initial charge-discharge curves of Bam-HC and Bam-PA-HC based cell. Inset is the comparison of the plateau and sloping capacity of Bam-HC and Bam-PA-HC based on the 2nd discharge/charge curves; g, Comparison of plateau capacity and initial coulombic efficiency between Bam-PA-HC and previously reported bamboo derived HCs [35–47].

showed an increased average pore size from 0.922 nm to 1.137 nm, indicating the enlargement of closed pores (Fig. 2e and Supplementary Fig. 5). This observation is further corroborated by the TEM images (Supplementary Fig. 6). Specifically, In Bam-1600, closed pores were rarely observed, whereas in Bam-PA-1600, numerous closed pores with diameters around 1 nm were clearly visible. Furthermore, Bam-PA-1600 exhibited enlarged interlayer spacing (0.396 nm) (Supplementary Fig. 7) and a higher A_D/A_G ratio (Supplementary Fig. 8) compared to Bam-1600, suggesting more disordered structure after being treated with PA.

It has been widely reported that closed pores are effective active sites for sodium storage at the low-voltage plateau[31,48]. Thus, massive closed pores in HC can effectively increase its reversible capacity. To prove it, the electrochemical performances of both Bam-1600 and Bam-PA-1600 through coin cells. Cell based on Bam-PA-1600 delivered higher charge specific capacity with 471.2 mAh g^{-1} than Bam-1600 (327.9 mAh g^{-1}) (Fig. 2f). Notably, the plateau capacity also increased by 65.95% after PA treatment (from 242.62 mAh g^{-1} to 402.63 mAh g^{-1}), which is better than all the bamboo-derived HC anodes (Fig. 2g and Supplementary Table 2). Besides, Bam-PA-1600 based cell showed excellent cycling stabilities with 94.4% of its initial capacity retention after 75 cycles at current density of 20 mA g^{-1} (Supplementary Fig. 9) and a 98.1% capacity retention after 80 cycles at 100 mA g^{-1} (Supplementary Fig. 10). Further, the full cell base on Bam-PA-1600 and $Na_3V_2(PO_4)_3$ can deliver a high discharge capacity 108.6 mAh g^{-1} (based on the mass of the cathode electrode), with a high capacity retention of 97.8% after 15 cycles (Supplementary Fig. 11).

2.2. PA recovery and recycling

Apart from its functionality as a deashing agent and pore former, PA also possessed other great merits for massive, sustainable and recyclable production of high-performance HC. Fig. 3a illustrated the fabrication of bamboo-derived HC based on recycled PA. Specifically, bamboo, initially, was crushed into powder and the obtained powder was leached with PA. Excess PA was then removed by vacuum filtration and collected for reuse and the PA-treated bamboo powder underwent a two-step carbonization process to obtained either HCs or other biocarbon (eg:

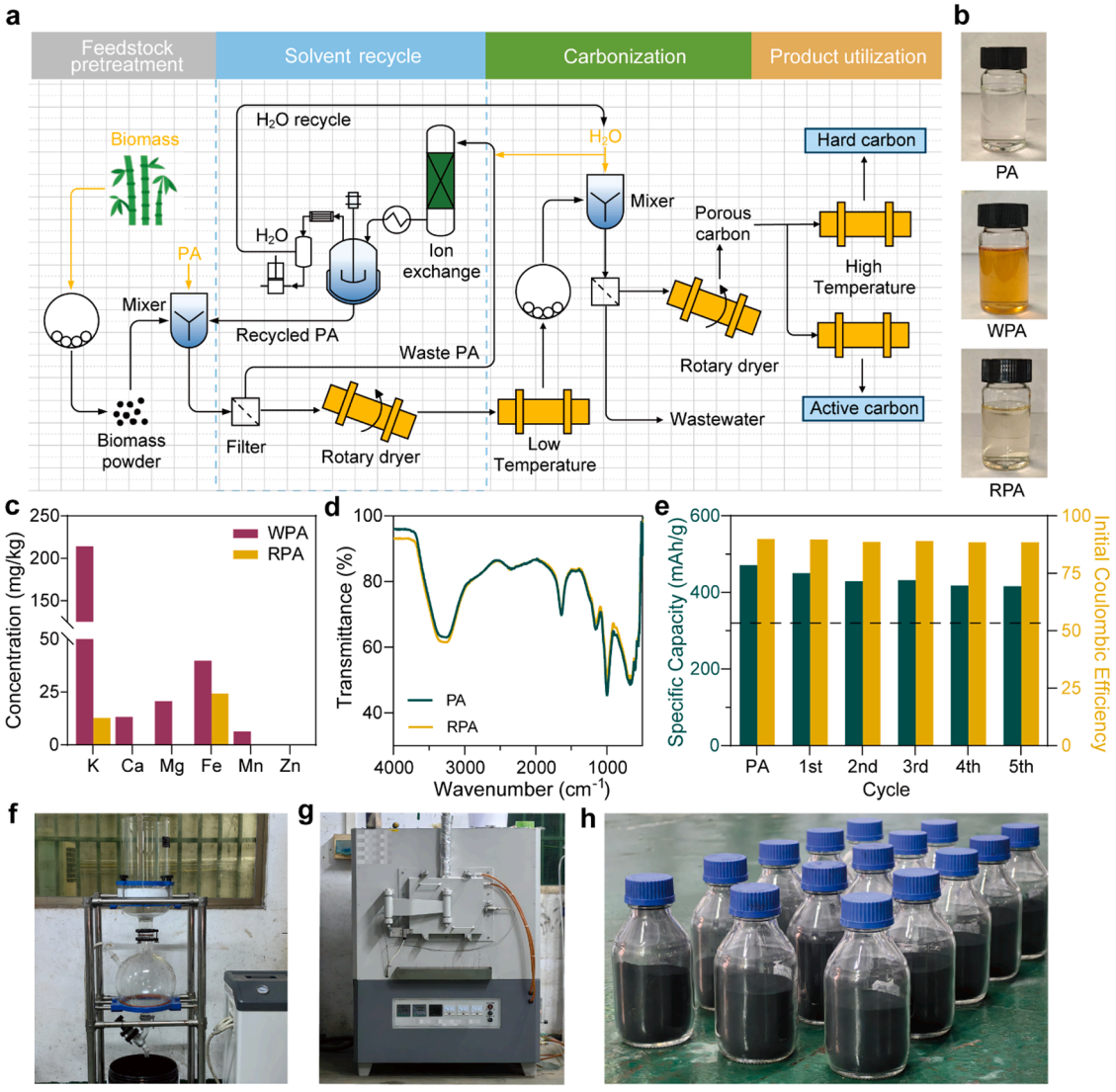

Fig. 3. . Recycling and characterization of PA.
a, Simplified process flow diagram of the PA-HC product and PA Recycling. A dashed blue boundary is shown the solvent recovery unit operations. b, Photos of PA, WPA and RPA. c, The content of various metal elements by ICP-OES of WPA and RPA. d, FTIR spectra of PA and RPA. e, The specific capacity and initial coulombic efficiency of HC from each PA recycling cycle. f, Photo of a 20 L filtration device. g, Muffle furnace used in initial large-scale Bam-HC production. h, Produced Bam-HC from the production test.

active carbon). And the collected wasted PA (WPA) was further deal with ion exchange to form usable recycled PA (RPA) with removing excess water through vacuum evaporation.

To evaluate the recyclability of PA, the WPA and RPA were further used to treat bamboo. It can be clearly seen that the RPA were pale-yellow, close to fresh PA, suggesting that most chromophoric organic compounds have been removed during regeneration and decolorization (Fig. 3b). And ICP-OES analysis confirmed that the contents of metallic elements in WPA originating from their chelation with PA decreased significantly, proving that most metal ions were removed during ion exchange (Fig. 3c). Besides, PA and RPA exhibited highly consistent FTIR (Fig. 3d) and ^{31}P NMR spectra (Supplementary Fig. 12), indicating their structural homogeneity. Moreover, the HC anodes obtained based on RPA also showed remarkably high reversible charge specific capacities and initial coulombic efficiencies. Specifically, even with 5 recycles, the obtained HC delivered high specific capacity (416 mAh/g) and outstanding ICE (88.5%) in initial cycle (Fig. 3e).

Furthermore, the industrial feasibility of the PA treatment was also evaluated through a pilot-scale manufacturing trial. Bamboo powder was reacted with PA in a 30 L reactor with ratio of 1:10 (solid: liquid); then, after excess PA was removed by vacuum filtration (Fig. 3f), the resulting solid was transferred to a 30 L atmosphere muffle furnace and

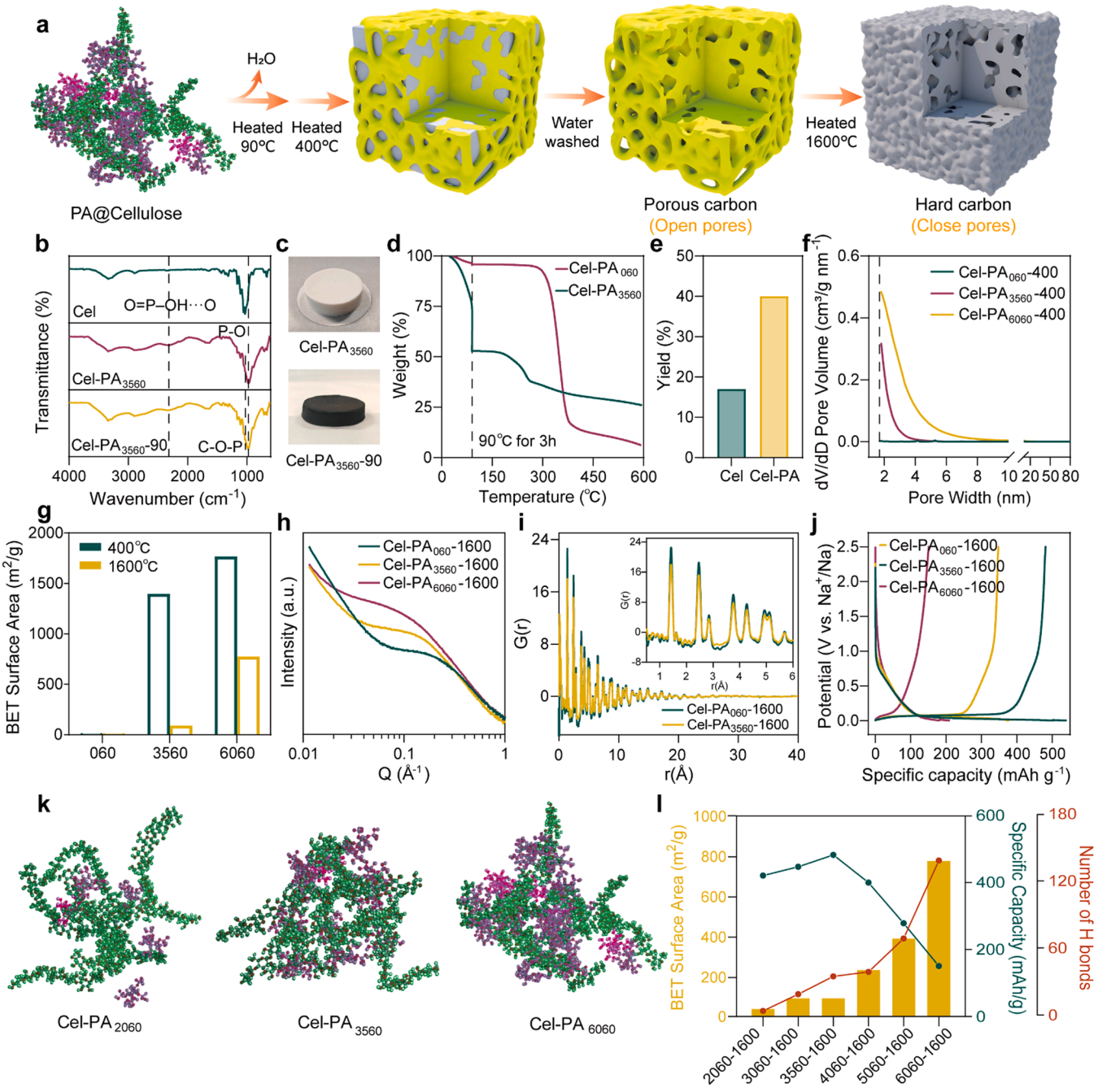

Fig. 4. . Fabrication and structure of hard carbon with closed-pores microspheres.
a, Schematic of the synthesis of Cel-PA-HC; b, FTIR spectra of Cel, Cel-PA$_{3560}$ and Cel-PA$_{3560}$–90; c, Photos of Cel-PA$_{3560}$ and Cel-PA$_{3560}$–90; d, TG curves of Cel-PA$_{060}$ and Cel-PA$_{3560}$; e, Carbon yield of Cel and Cel-PA (from precursors to HC); f, Pore size distribution of Cel-PA$_{060}$–1600, Cel-PA$_{3560}$–1600 and Cel-PA$_{6060}$–1600; g, BET surface area of samples; h, Long-range and enlarged profiles of PDF; i, Small-angle X-ray scattering patterns; j, Galvanostatic charge-discharge curves for the first cycle; k, Mixed state of Cellulose chain and PA after 500 ps simulation; l, BET surface area, Specific capacity and Number of H-bonds between PA of samples.

subjected to two-step carbonization. (Fig. 3g). Finally, HC was collected after the calcined powder washing. This scale-up process enables kilogram-scale batch production of bamboo-derived HC (Fig. 3h).

2.3. Mechanistic investigation of pore formation

Lignocellulose, one of the most abundant biomass resources on the earth, is composed of cellulose (40–50%), hemicellulose (15–30%), and lignin (15–25%), along with minor proteins, lipids, and ash [49–50]. Given the complexity of biomass, it is difficult to directly investigate PA's working mechanism during HC fabrication process. Considering fractions of cellulose and hemicellulose in lignocellulose and their similar structural units, cellulose was selected as a target for mechanism analysis.

For the formation of high-performance biomass-derived HC with PA treatment, we proposed a four-step process shown in Fig. 4a. 1) PA penetrated into cellulose matrix and catalyzed the hydrolysis of cellulose into oligosaccharides, forming a uniform PA@cellulose mixture; 2) PA catalyzed cellulose dehydration at 90 °C and *in situ*-formed polyphosphoric acids acted as molten sacrificial templates to prevent pore collapse during subsequent low-temperature carbonization; 3) A porous carbon matrix was obtained with removing phosphorus compounds via water; 4) Lastly, the further high-T carbonization converted the massive open pores into closed pores, forming the closed pores-rich HCs. To evident it, systematic tests were conducted, including Fourier Transform Infrared Spectroscopy (FT-IR), Thermogravimetric Analysis (TGA), Brunauer-Emmett-Teller Method (BET), Neutron pair distribution function (nPDF), and molecular dynamics (MD) simulations.

The FT-IR spectra of cellulose and PA@cellulose mixture were shown in Fig. 4b, it can be clearly seen that an extra peak emerged at 2310 cm^{-1} in Cel-PA_{3560} and Cel-PA_{3560}–90, relating to the hydrogen-bonding interaction between PA and cellulose. It was also evidenced by SSNMR result (Supplementary Fig. 13). Specifically, during heating treatment process, a noticeable color change from white to black was observed after being heated at 90 °C for 12 h, originating from the cellulose dehydration (Fig. 4c). To further quantify the carbonization process, TGA for both cellulose and Cel-PA_{3560} were conducted (Fig. 4d) and the results showed that compared to the limited mass loss (~ 4%) for pristine cellulose, Cel-PA_{3560} undergoes a substantial mass loss (48%) after 3 h at 90 °C, which probably from likely reflecting PA-promoted dehydration of cellulose (15.8%) and water in PA solution (32.2%). Furthermore, The DTG curve (Supplementary Fig. 14) showed that the pristine cellulose started to decompose at 300 °C, while the decomposition temperature shifted to 200 °C for Cel-PA_{3560}. Additionally, TG-MS results (Supplementary Fig. 15) revealed that Cel-PA delivered less CO_2 emission during the carbonization process, resulting to higher yield from 17% to 40%, close to its theoretical value (44.44%), which is even comparable to that of resin precursors (Fig. 4e and 2d).

To evaluate the carbon matrix after low temperature carbonization, BET measurements were performed and the results were shown in Fig. 4f and Supplementary Fig. 16. The N_2 adsorption-desorption isotherm of Cel-PA_{3560}–400 showed a typical type-I isotherm, indicating the presence of abundant micropores (<2 nm). In contrast, Cel-PA_{6060}–400 exhibited a combined Type-I and H2(a) isotherm, revealing the existence of micropores and "ink-bottle" shape pores. Moreover, Compared with Cel-PA_{6060}–400, Cel-PA_{3560}–400 exhibited smaller and more uniform pores, which facilitates pore closure during high-temperature carbonization. And the SSA of PA treated samples increased significantly from 7.03 m^2/g to 1397.24 m^2/g). As expected, pristine cellulose continued to exhibit low SSA after high-temperature carbonization (Fig. 4g). Notably, the SSA of Cel-PA_{3560}–400 decreases significantly from 1397.24 m^2/g to 90.38 m^2/g. In contrast, the N_2 adsorption–desorption isotherm of Cel-PA_{6060}–1600 continued to exhibit a combined Type I and H_2(a) isotherm (Supplementary Fig. 17), suggesting that the "ink-bottle" shape pores remained and pores were not effectively sealed during carbonization, which contributed to its high SSA (775.61 m^2/g).

To investigate micropores (< 1 nm), CO_2 adsorption–desorption tests were further conducted (Supplementary Fig. 18). The results revealed that both Cel-PA_{3560}–1600 and Cel-PA_{6060}–1600 exhibited massive micropores with size of ~ 0.8 nm. Interestingly, despite significant differences in their N_2-SSA, their CO_2-SSA and pore volumes were quite similar, which indicated that both possessed similar microporous structures. The huge difference on N_2-SSA originated from the pore-surface connection. In Cel-PA_{6060}–1600, pores were connected to the external surface through larger openings, which showed high SSA values in N_2 test; In contrast, pores in Cel-PA_{3560}–1600 remained enclosed and less accessible. And this pore connection difference may be attributed to the relatively larger pores formation during low-temperature carbonization, which further impeded the effective closure of open structures during subsequent high-temperature treatment.

This observation was further evident by the TEM results. In Cel-PA_{060}–1600, closed pores were rarely observed, whereas in Cel-PA_{3560}–1600, numerous closed pores around 1 nm were clearly visible. Additionally, as the concentration of PA increased, larger open pores were observed in sample Cel-PA_{6060}–1600 (Supplementary Fig. 19). Moreover, their SAXS patterns (Fig. 4h) also showed increased scattering intensities in the range of 0.1–0.2 $Å^{-1}$ with increasing PA concentration, proving the enlargement of closed pores. And their fitting results further confirmed the increased pore sizes (Supplementary Fig. 20).

To betterer understand their chemical bonding information, nPDF measurements[51] and Raman spectroscopy tests were performed. The obtained G(r) results (Fig. 4i) revealed that both Cel-PA_{060}–1600 and Cel-PA_{3560}–1600 were dominated by sp^2-coordinated aromatic carbon, while the absence of a sharp interlayer peak at 3.35–3.45 Å indicated their turbostratic stacking structure. Cel-PA_{060}–1600 exhibited sharper and stronger peaks in the first three features within 1–3 Å, suggesting it possesses higher degree of local sp^2 ordering and a narrower bond-length distribution. In contrast, the broader and slightly weaker peaks observed in Cel-PA_{3560}–1600 reflected its more local structural disorder. In the range of 6–40 Å, both samples displayed damped oscillations that decayed to the baseline around ~20–25 Å. The similar envelope and phase implied comparable correlation lengths of the nanodomains (~1.5–2.5 nm). Besides, Raman spectroscopy results (Supplementary Fig. 21) showed that both spectra can be well deconvoluted into five peaks, including I, D, D", G and D'. Among them, G peak at ~1580 cm^{-1} and D peak at 1340–1360 cm^{-1} can be assigned to the E_{2g}-symmetry vibration mode of ideal graphitic lattice and the A_{1g}-symmetry vibration mode of defective graphitic lattice, respectively. The increased A_D/A_G ratio represented that PA promoted the formation of more disordered carbon structures. Moreover, graphitic phase can also be evident by broad peaks at low angles (2θ=21–23°) in XRD patterns (Supplementary Fig. 22), which can be assigned to (002). And the calculated values of interlayer spacing showed that Cel-PA_{3560}–1600 exhibited a larger interlayer spacing of 0.396 nm compared to Cel-PA_{060}–1600 (0.388 nm).

The electrochemical performance of HCs treated with various contents of PA was evaluated through half-cell test. Cel-PA_{3560}–1600 exhibited a remarkably reversible specific capacity of 483 mAh/g and an ICE of 90% (Fig. 4j) due to its abundant closed-pore structure. However, Cel-PA_{6060}–1600, with massive micropores, only delivered limited reversible specific capacity of 151 mAh/g and an ICE of 72%, which originated from the connection between pores and external surface through open channels. This connection was detrimental to store sodium ions. Additionally, the excessively large surface area promoted electrolyte decomposition during cycling, resulting in low ICE.

To uncover the relationship between pore structure and capacity of HCs, a series of PA concentrations were further investigated. The BET and Raman results showed that both SSA and A_D/A_G ratio of the HC with PA concentration increasing (Supplementary Figs. 23 and 24), While the reversable capacity increased, reached an optimum at 3560 and then

declined sharply with concentration kept increasing (Supplementary Figs. 25–27 and Supplementary Table 3). To elucidate this trend, MD simulations were performed to analyze hydrogen bonding between PA-PA and PA-Cellulose pairs. Hydrogen bonds were identified according to two geometric criteria: (1) the distance between donor and acceptor atoms was <3.5 Å, and (2) the angle formed by the hydrogen, donor, and acceptor atoms was smaller than 30° Only those hydrogen bonds that can meet both criteria were counted. The temporal evolution of the hydrogen-bond obtained under these criteria was presented in Supplementary Fig. 28. The number of hydrogen bonds between PA molecules decreased rapidly at the beginning of the simulation and then reached equilibrium, whereas the number of hydrogen bonds between PA and Cellulose rose sharply initially and subsequently stabilized. These results suggest that during leaching process, PA molecules penetrated between cellulose chains, thereby weakening the intermolecular hydrogen bonding among PA molecules. After 500 ps of MD simulation, the cellulose chains became twisted, and the PA molecules were uniformly distributed between them (Supplementary Fig. 29). At low concentrations, PA molecules were separated by cellulose chains, resulting in limited intermolecular interactions; with concentration increasing, aggregation of PA molecules occurred (Fig. 4k). Massive PA-PA hydrogen bonds formed significantly with PA concentration reached 29.2% (PA-3560), closely paralleling to the variation in the SSA of the resulting HC (Fig. 4l).

Here, we propose a possible mechanism for this phenomenon. When PA concentration is lower than the critical value, PA molecules are dispersed within the cellulose matrix without significant intermolecular interactions, forming uniformly distributed closed pores after carbonization. However, PA concentration increases and surpasses the critical value, stronger interactions among PA molecules promote the formation

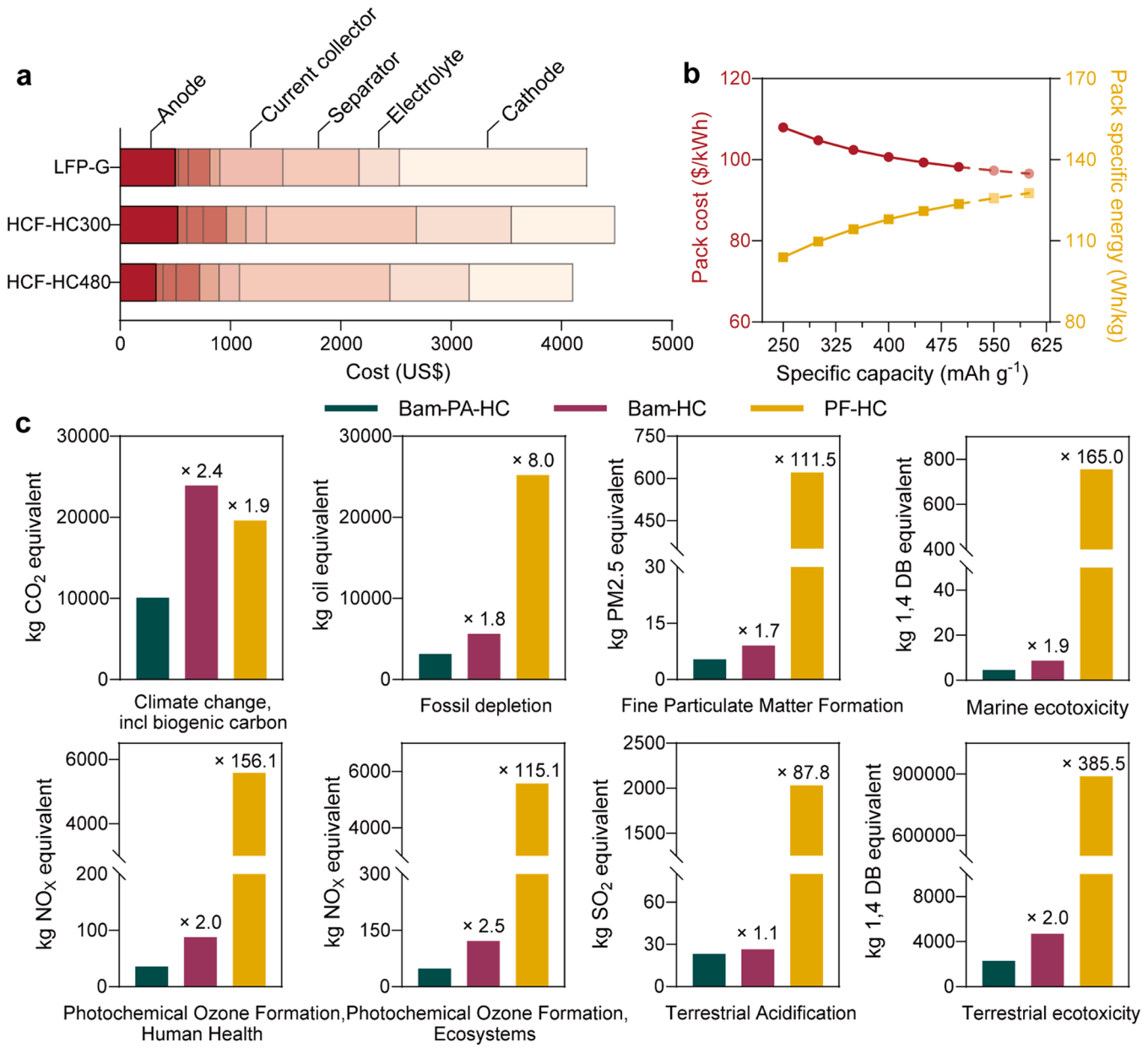

Fig. 5. . Cost analysis of batteries fabrication and environmental impact of HC production.
a, Total and component cost breakdown for a 100 kWh, 150 kW battery pack, including Graphite//LFP, Bam-HC//HCF and Bam-PA-HC//HCF. **b,** Variation of battery pack energy cost and energy density with HC Capacity. **c,** Comparative analysis of the environmental impacts associated with the Bam-PA-HC as opposed to Bam-HC and PF-HC. Dichlorobenzene (1,4-DB), which is a well-known pesticide, is used as a reference substance for normalizing the toxicity of the other substances contributing in this impact category.

of larger, interconnected pores, which are detrimental to sodium-ion storage.

2.4. Battery cost analysis and LCA of HC production

It is widely recognized that SIBs are more cost-effective than lithium-ion batteries (LIBs) due to the absence of expensive elements such as Li, Ni, and Co[52–53]. However, the low capacity of HC anodes partially offsets the cost advantage from cathode materials, while the increased consumption of other components (e.g., electrolyte, separator) further contributes to the overall cost increase[54]. To quantify the impact of HC reformation on SIBs costs, we employed Battery Performance and Cost (BatPac) 5.2 to model a 150 kW/100 kWh battery pack for premium electric vehicles and conducted a comprehensive cost breakdown analysis of its components (Fig. 5a), relevant parameters are listed in Supplementary Table 4. The calculated results showed that the Bam-PA-HC significantly enhanced capacity while reducing production costs. However, high porosity of HC and limited capacity & low density of Prussian-type cathode resulted in more use of electrolytes and separator, which greatly increases the cost of SIBs, even higher than commercial LIBs based on lithium iron phosphate (LFP) and Graphite (G).

As shown in Fig. 5b, as the HC capacity increased, the energy density of the battery pack rose while the cost decreased. However, when the capacity exceeded 500 mAh g^{-1}, the rate of increase diminishes due to diminishing returns. Accordingly, targeting a HC capacity around 500 mAh g^{-1} is likely more cost-effective than pursuing ever-higher capacities.

Moreover, except for its cost-effectiveness and high capacity, the massive production process of Bam-PA-HC also possesses green and sustainable merits, compared to phenolic resin-based HC (PF-HC) and traditional biomass-based HC, suffering from high cost and required additional purification, respectively. To further evaluate its environmental impact, a Life Cycle Assessment (LCA) was conducted (Supplementary Figs. 30–35). And the results indicated that Bam-PA-HC achieved the lowest greenhouse gas (GHG) emissions—57.83% lower than those for Bam-HC. Unexpectedly, even with bamboo's carbon sequestration effect, the GHG emissions of Bam-HC were slightly higher than those of PF-HC (Fig. 5c). This disparity was mainly attributable to HCl and NaOH consumptions during deashing and wastewater treatment processes, respectively, which mainly accounted for GHG emissions. Notably, although carbonization off-gas is typically reused as fuel in actual production, this recovery process was excluded from our model for simplicity, potentially leading to an overestimation of GHG emissions. Among the varieties of the examined environmental impact categories, the Bam-PA-HC demonstrated lower impacts compared with the other two methods, including fossil depletion, fine particulate matter formation, terrestrial acidification. Moreover, the fabrication of PF-HC may contribute to ecotoxicity, with marine and terrestrial ecotoxicity being 165.0 and 386.5 times higher, compared with the Bam-PA-HC, respectively. All these results firmly supported the environmental sustainability of the PA mediated HC production process.

3. Conclusion

In this work, we developed a cost-effective, green, sustainable method for preparing high-performance biocarbon through recyclable bio-acid (phytic acid) and validated its effectiveness as SIBs anodes. Precise regulations on pore's structures were achieved through controlling PA dispersion within lignocellulose matrix and massive closed pores were constructed in biomass-derived HC. Consequently, the optimized HC exhibited an excellent performance with high capacity (483.1 mAh g^{-1}) and superb reversibility (ICE: 90%).

And the sustainability implications of the proposed bioacid-mediated method are twofold. Firstly, raw materials (PA and bamboo) are derived from biomass, avoiding the use of highly polluting chemicals such as hydrochloric acid and phenol-formaldehyde resins. Secondly, in terms of solvent recyclability, PA demonstrates impressive reusability, underscoring its recyclability and economic feasibility. The LCA results further highlight its environmental friendliness, indicating a reduction in the environmental footprint associated with production.

Our work provides fundamental insights and guidance for the high-performance HC massive production based on biomass through green, sustainable paths.

CRediT authorship contribution statement

Xinlin Shi: Writing – review & editing, Writing – original draft, Visualization, Validation, Methodology, Investigation, Data curation. **Guobiao Jin:** Writing – review & editing, Visualization, Methodology, Investigation, Data curation. **Jie Lin:** Writing – review & editing, Validation, Methodology, Investigation, Data curation. **Feng Jin:** Writing – review & editing, Writing – original draft, Supervision, Methodology. **Rui Liu:** Writing – review & editing, Methodology, Investigation, Data curation. **Lu Wang:** Writing – review & editing, Methodology, Investigation. **Yumeng Lan:** Writing – review & editing, Methodology, Investigation. **Zhihao Shen:** Writing – review & editing, Methodology, Investigation, Data curation. **Qimin Tian:** Writing – review & editing, Validation, Investigation. **Hongzhou Lu:** Writing – review & editing, Investigation. **Xinjun Qian:** Writing – review & editing, Investigation. **Qingsong Wang:** Writing – review & editing, Investigation. **Keao Wu:** Writing – review & editing, Investigation. **Junping Jia:** Resources, Methodology, Investigation, Data curation. **Haipeng Yang:** Resources, Methodology, Investigation, Data curation. **Hai Lin:** Supervision, Resources, Methodology, Investigation. **Zirui Lou:** Writing – review & editing, Writing – original draft, Supervision, Resources, Methodology, Investigation, Funding acquisition, Data curation. **Feng Pan:** Writing – review & editing, Validation, Supervision, Resources, Methodology, Investigation, Funding acquisition.

Declaration of competing interest

The authors declare that they have no known competing financial interests or personal relationships that could have appeared to influence the work reported in this paper.

Acknowledgement

We gratefully acknowledge the financial support received from National Natural Science Foundation of China (Grant No 92472206), National Center for International Research of Power Batteries and Materials (No. 2015B01015), Guangdong Key Laboratory of Design and Calculation of New Energy Materials (No. 2017B030301013), Shenzhen Key Laboratory of New Energy Resources Genome Preparation and Testing (No. ZDSYS201707281026184), the Key Project of Basic Research of the Shenzhen Natural Science Foundation (JCYJ20241202125901003), Major Science and Technology Infrastructure Project of Material Genome Big-science Facilities Platform supported by Municipal Development and Reform Commission of Shenzhen. Additionally, we thank the staff members of the Multi-Physics Instrument (https://cstr.cn/31113.02.CSNS.MPI) at the China Spallation Neutron Source (CSNS) (https://cstr.cn/31113.02.CSNS), for providing technical support and assistance in data collection and analysis.

Supplementary materials

Supplementary material associated with this article can be found, in the online version, at doi:10.1016/j.ensm.2026.105101.

Data availability

Data will be made available on request.

References

[1] Z. Zhu, T. Jiang, M. Ali, Y. Meng, Y. Jin, Y. Cui, W. Chen, Rechargeable batteries for grid scale energy storage, Chem. Rev. 122 (2022) 16610–16751, https://doi.org/10.1021/acs.chemrev.2c00289.

[2] T. Jiang, D. Shen, Z. Zhang, H. Liu, G. Zhao, Y. Wang, S. Tan, R. Luo, W. Chen, Battery technologies for grid-scale energy storage, Nat. Rev. Clean Technol. 1 (2025) 474–492, https://doi.org/10.1038/s44359-025-00067-9.

[3] H. Li, Q. Yan, J. Li, J. Qiu, H. Zhang, Porous carbon materials: from traditional synthesis, machine learning-assisted design, to their applications in advanced energy storage and conversion, Adv. Funct. Mater. 35 (2025) 2504272, https://doi.org/10.1002/adfm.202504272.

[4] W.-J. Liu, H. Jiang, H.-Q. Yu, Emerging applications of biochar-based materials for energy storage and conversion, Energy Environ. Sci. 12 (2019) 1751–1779, https://doi.org/10.1039/C9EE00206E.

[5] C. Wu, Y. Yang, Y. Zhang, H. Xu, W. Huang, X. He, Q. Chen, H. Dong, L. Li, X. Wu, S. Chou, Industrial-scale hard carbon designed to regulate electrochemical polarization for fast sodium storage, Angew. Chem. Int. Edit. 63 (2024) e202406889, https://doi.org/10.1002/anie.202406889.

[6] S. Yu, J. He, Z. Zhang, Z. Sun, M. Xie, Y. Xu, X. Bie, Q. Li, Y. Zhang, M. Sevilla, M.-M. Titirici, H. Zhou, Towards negative emissions: hydrothermal carbonization of biomass for sustainable carbon materials, Adv. Mater. 36 (2024) 2307412, https://doi.org/10.1002/adma.202307412.

[7] J. Huang, Z. Huang, C. Zhang, T. Hao, T. Wang, D. Deng, Z. Sun, Y. Wang, C. Xu, J. Zeng, S. Tang, C. Huang, L. Yang, X. Wang, Monolithic carbon derived from biomass via zinc-assisted pyrolysis for lithium–sulfur batteries, Green Chem 27 (2025) 3326–3334, https://doi.org/10.1039/D4GC05753H.

[8] L. Leng, Q. Xiong, L. Yang, H. Li, Y. Zhou, W. Zhang, S. Jiang, H. Li, H. Huang, An overview on engineering the surface area and porosity of biochar, Sci. Total Environ. 763 (2021) 144204, https://doi.org/10.1016/j.scitotenv.2020.144204.

[9] J.L. Míguez, J. Porteiro, F. Behrendt, D. Blanco, D. Patiño, A. Dieguez-Alonso, Review of the use of additives to mitigate operational problems associated with the combustion of biomass with high content in ash-forming species, Renew. Sust. Energ. Rev. 141 (2021) 110502, https://doi.org/10.1016/j.rser.2020.110502.

[10] C. Wu, W. Huang, Y. Zhang, Q. Chen, L. Li, Y. Zhang, X. Wu, S.-L. Chou, Revisiting the critical role of metallic ash elements in the development of hard carbon for advancing sodium-ion battery applications, eScience 5 (2025) 100371, https://doi.org/10.1016/j.esci.2025.100371.

[11] Y. Hu, M. Yang, Q. Dong, X. Zou, J. Yu, S. Guo, F. Yan, Green and sustainable recycling of lithium-ion batteries via an ionic liquid-driven cathode reduction method, Energy Environ. Sci. 17 (2024) 4238–4247, https://doi.org/10.1039/D4EE00331D.

[12] X. Ma, Z. Meng, M.V. Bellonia, J. Spangenberger, G. Harper, E. Gratz, E. Olivetti, R. Arsenault, Y. Wang, The evolution of lithium-ion battery recycling, Nat. Rev. Clean Technol. 1 (2025) 75–94, https://doi.org/10.1038/s44359-024-00010-4.

[13] J. Cui, P. Su, W. Li, X. Wang, Y. Zhang, Z. Xiao, Q. An, Z. Chen, Advanced cellulose-derived hard carbon as anode for sodium-ion batteries: mechanisms, optimization, and challenges, Adv. Energy Mater. 15 (2025) 2404604, https://doi.org/10.1002/aenm.202404604.

[14] B. Pei, H. Yu, L. Zhang, G. Fang, J. Zhou, X. Cao, S. Liang, Hard carbon for sodium-ion batteries: from fundamental research to practical applications, Adv. Mater. 37 (2025) 2504574, https://doi.org/10.1002/adma.202504574.

[15] J. Duan, Z. Xu, M. Li, P. Yang, H. Hu, Z. Zhang, Z. Chen, Y. Jiang, J. Zhang, Structure regulation of hard carbon with enriched semi-closed ultramicropores for enhanced rapid sodium storage, Adv. Funct. Mater. 35 (2025) 2508822, https://doi.org/10.1002/adfm.202508822.

[16] W. Deng, Y. Wang, Z. Chen, H. Huang, C. Chen, B. Pan, Y. Yang, S. He, H. Pan, H. Yang, Y. Yu, Catalyst-assisted chemical vapor deposition engineering of hard carbon with abundant closed pores for high-performance sodium-ion batteries, Adv. Funct. Mater. 35 (2025) 2501721, https://doi.org/10.1002/adfm.202501721.

[17] Z. Tang, R. Zhang, H. Wang, S. Zhou, Z. Pan, Y. Huang, D. Sun, Y. Tang, X. Ji, K. Amine, M. Shao, Revealing the closed pore formation of waste wood-derived hard carbon for advanced sodium-ion battery, Nat. Commun. 14 (2023) 6024, https://doi.org/10.1038/s41467-023-39637-5.

[18] J. Peng, H. Wang, X. Shi, H.J. Fan, Ultrahigh plateau-capacity sodium storage by plugging open pores, Adv. Mater. 37 (2025) 2410326, https://doi.org/10.1002/adma.202410326.

[19] D. Igarashi, Y. Tanaka, K. Kubota, R. Tatara, H. Maejima, T. Hosaka, S. Komaba, New template synthesis of anomalously large capacity hard carbon for Na- and K-ion batteries, Adv. Energy Mater. 13 (2023) 2302647, https://doi.org/10.1002/aenm.202302647.

[20] Q. Li, X. Liu, Y. Tao, J. Huang, J. Zhang, C. Yang, Y. Zhang, S. Zhang, Y. Jia, Q. Lin, Y. Xiang, J. Cheng, W. Lv, F. Kang, Y. Yang, Q.-H. Yang, Sieving carbons promise practical anodes with extensible low-potential plateaus for sodium batteries, Natl. Sci. Rev. 9 (2022) nwac084, https://doi.org/10.1093/nsr/nwac084.

[21] S. Ding, W. Cheng, L. Zhang, G. Du, X. Hao, G. Nie, B. Xu, M. Zhang, Q. Su, C. A. Serra, Organic molecule confinement reaction for preparation of the Sn nanoparticles@graphene anode materials in lithium-ion battery, J. Colloid Interface Sci. 589 (2021) 308–317, https://doi.org/10.1016/j.jcis.2020.12.086.

[22] J. Liu, Y. You, L. Huang, Q. Zheng, Z. Sun, K. Fang, L. Sha, M. Liu, X. Zhan, J. Zhao, Y.-C. Han, Q. Zhang, Y. Chen, S. Wu, L. Zhang, Precisely tunable instantaneous carbon rearrangement enables low-working-potential hard carbon toward sodium-ion batteries with enhanced energy density, Adv. Mater. 36 (2024) 2407369, https://doi.org/10.1002/adma.202407369.

[23] Y. Qiu, Y. Su, X. Jing, H. Xiong, D. Weng, J.-G. Wang, F. Xu, H. Wang, Rapid closed pore regulation of biomass-derived hard carbons based on flash joule heating for enhanced sodium ion storage, Adv. Funct. Mater. 35 (2025) 2423559, https://doi.org/10.1002/adfm.202423559.

[24] W. Zhang, Y. Du, Y. Qiu, C. Li, I. Razanau, A. Kaisha, F. Xu, H. Wang, Closed-pore engineering in hard carbon for sodium ion storage: advances, challenges and future horizons, Adv. Energy Mater. 15 (2025) e03884, https://doi.org/10.1002/aenm.202503884.

[25] Y. Qiu, G. Jiang, Y. Su, X. Zhang, Y. Du, X. Xu, Q. Ye, J. Zhang, M. Ban, F. Xu, H. Wang, Hybrid hard carbon framework derived from polystyrene bearing distinct molecular crosslinking for enhanced sodium storage, Carbon Energy 6 (2024) e479, https://doi.org/10.1002/cey2.479.

[26] Y. Zhang, Z. Zhou, Q. Lin, Q. Jing, Z. Wang, S. Yan, J. Guo, Y. Shuai, L. Fan, Open sesame: tailoring the microstructure of biomass-derived hard carbon for high-efficiency sodium-ion battery anodes, Chem. Eng. J. 515 (2025) 163768, https://doi.org/10.1016/j.cej.2025.163768.

[27] Z. Zhou, Z. Wang, Y. Zhang, Q. Lin, Y. Shuai, L. Fan, Rational design of hard carbon anodes for sodium-ion batteries: precursor engineering, structural modulation and industrial scalability, Energy Storage Mater 80 (2025) 104443, https://doi.org/10.1016/j.ensm.2025.104443.

[28] Y. Zhang, Z. Zhou, Q. Lin, Q. Zhang, L. Fan, Precise decoupling of biomass components to engineer hard carbon microcrystalline architecture for enhanced sodium-ion storage performance, Small 21 (2025) e07313, https://doi.org/10.1002/smll.202507313.

[29] X. Qiao, G. Jin, R. Liu, J. Hou, X. Shi, L. Wang, Q. Tian, H. Lu, Z. Shen, Y. Lan, Z. Lou, F. Pan, A function-oriented binder with exceptional interface ion transport and impurity tolerance for hard carbon anode, Small 21 (2025) 2500532, https://doi.org/10.1002/smll.202500532.

[30] J. Zhao, X.-X. He, W.-H. Lai, Z. Yang, X.-H. Liu, L. Li, Y. Qiao, Y. Xiao, L. Li, X. Wu, S.-L. Chou, Catalytic defect-repairing using manganese ions for hard carbon anode with high-capacity and high-initial-coulombic-efficiency in sodium-ion batteries, Adv. Energy Mater. 13 (2023) 2300444, https://doi.org/10.1002/aenm.202300444.

[31] Z. Zheng, S. Hu, W. Yin, J. Peng, R. Wang, J. Jin, B. He, Y. Gong, H. Wang, H.J. Fan, CO2-Etching creates abundant closed pores in hard carbon for high-plateau-capacity sodium storage, Adv. Energy Mater. 14 (2024) 2303064, https://doi.org/10.1002/aenm.202303064.

[32] S.C. Dey, B. Worfolk, L. Lower, W.J. Sagues, M.R. Nimlos, S.S. Kelley, S. Park, Phenolic resin derived hard carbon anode for sodium-ion batteries: a review, ACS Energy Lett 9 (2024) 2590–2614, https://doi.org/10.1021/acsenergylett.4c00688.

[33] A. Beda, P.-L. Taberna, P. Simon, C. Matei Ghimbeu, Hard carbons derived from green phenolic resins for Na-ion batteries, Carbon 139 (2018) 248–257, https://doi.org/10.1016/j.carbon.2018.06.036.

[34] A. Kamiyama, K. Kubota, T. Nakano, S. Fujimura, S. Shiraishi, H. Tsukada, S. Komaba, High-capacity hard carbon synthesized from macroporous phenolic resin for sodium-ion and potassium-ion battery, ACS Appl. Energ. Mater. 3 (2020) 135–140, https://doi.org/10.1021/acsaem.9b01972.

[35] Y. Leng, S. Dong, Z. Chen, Y. Sun, Q. Xu, L. Ma, X. He, C. Hai, Y. Zhou, Preparation of high-performance anode materials for sodium-ion batteries using bamboo waste: achieving resource recycling, J. Power Sources 613 (2024) 234826, https://doi.org/10.1016/j.jpowsour.2024.234826.

[36] N. Lan, Y. Shen, J. Li, H. He, C. Zhang, Cell-shearing chemistry directed closed-pore regeneration in biomass-derived hard carbons for ultrafast sodium storage, Adv. Mater. 37 (2025) 2412989, https://doi.org/10.1002/adma.202412989.

[37] Y. Wang, Z. Yi, S. Zhang, Y. Mao, L. Li, H. Liu, Z. Liu, L. Xie, F. Su, Lowering energy barriers of free radicals facilitates defect-suppressed carbon layers of hard carbon, Small 21 (2025) e06923, https://doi.org/10.1002/smll.202506923.

[38] Y. Wang, Z. Yi, L. Xie, Y. Mao, W. Ji, Z. Liu, X. Wei, F. Su, C.-M. Chen, Releasing free radicals in precursor triggers the formation of closed pores in hard carbon for sodium-ion batteries, Adv. Mater. 36 (2024) 2401249, https://doi.org/10.1002/adma.202401249.

[39] J. Kuai, J. Xie, J.D. Wang, J.Y. Chen, J. Wang, F. Liu, X.W. Xu, J. Tu, J.P. Cheng, Optimizing hard carbon materials for sodium-ion batteries: insights from particle size and soft carbon-coating strategy, J. Power Sources 627 (2025) 235792, https://doi.org/10.1016/j.jpowsour.2024.235792.

[40] M. Li, J. Hu, L. Xu, G. Liu, Y. Sun, Y. Lei, X. Zhang, L. Zhang, X. Li, Multi-synergistic regulation of hard carbon via a green bioengineering strategy to achieve high-capacity sodium-ion storage, Green Chem 27 (2025) 2696–2705, https://doi.org/10.1039/D4GC05497K.

[41] Z. Sun, Z. Li, Y. Li, Z. Wang, H. Zuo, L. Zhao, X. Liu, Unveiling a two-stage closed-pore formation mechanism in bamboo-derived hard carbons for high-plateau-capacity sodium-ion battery anodes, Chem. Eng. J. 521 (2025) 167011, https://doi.org/10.1016/j.cej.2025.167011.

[42] Z. Huang, J. Huang, L. Zhong, W. Zhang, X. Qiu, Deconstruction engineering of lignocellulose toward high-plateau-capacity hard carbon anodes for sodium-ion batteries, Small 20 (2024) 2405632, https://doi.org/10.1002/smll.202405632.

[43] W. Zhao, S. Zhang, H. Lai, W. He, B.K. Yap, U. Feleni, X. Peng, J. Cui, L. Zhong, A dual-phase pore engineering strategy to enhance low-voltage plateau capacity of hard carbon for sodium-ion batteries, Carbon Energy 7 (2025) e70047, https://doi.org/10.1002/cey2.70047.

[44] Z. Tang, R. Liu, D. Jiang, S. Cai, H. Li, D. Sun, Y. Tang, H. Wang, Regulating the pore structure of biomass-derived hard carbon for an advanced sodium-ion battery, ACS Appl. Mater. Interfaces 16 (2024) 47504–47512, https://doi.org/10.1021/acsami.4c08082.

[45] T. Xu, X. Qiu, X. Zhang, Y. Xia, Regulation of surface oxygen functional groups and pore structure of bamboo-derived hard carbon for enhanced sodium storage

performance, Chem. Eng. J. 452 (2023) 139514, https://doi.org/10.1016/j.cej.2022.139514.
[46] C. Wu, Y. Yang, Y. Li, X. He, Y. Zhang, W. Huang, Q. Chen, X. Liu, S. Chen, Q. Gu, L. Li, S.C. Smith, X. Tan, Y. Yu, X. Wu, S. Chou, Unraveling the structure–performance relationship in hard carbon for sodium-ion battery by coupling key structural parameters, Energy Environ. Sci. 18 (2025) 6019–6031, https://doi.org/10.1039/D5EE00278H.
[47] C.-C. Li, Y.-L. Wang, Z.-L. Yi, F. Yang, R.-H. Niu, F.-Y. Su, Y.-P. Wang, Z.-F. Liu, Z.-W. Wu, L.-J. Xie, C.-M. Chen, Enhanced Na storage performance through in situ depolymerization–repolymerization in bamboo-derived hard carbon anodes, J. Mater. Chem. A 13 (2025) 16533–16546, https://doi.org/10.1039/D5TA00439J.
[48] X. Chen, J. Tian, P. Li, Y. Fang, Y. Fang, X. Liang, J. Feng, J. Dong, X. Ai, H. Yang, Y. Cao, An overall understanding of sodium storage behaviors in hard carbons by an "adsorption-intercalation/filling" hybrid mechanism, Adv. Energy Mater. 12 (2022) 2200886, https://doi.org/10.1002/aenm.202200886.
[49] V. Sharma, M.-L. Tsai, P. Nargotra, C.-W. Chen, P.-P. Sun, R.R. Singhania, A. K. Patel, C.-D. Dong, Journey of lignin from a roadblock to bridge for lignocellulose biorefineries: a comprehensive review, Sci. Total Environ. 861 (2023) 160560, https://doi.org/10.1016/j.scitotenv.2022.160560.
[50] Z. Lv, X. Yan, S. Jia, J. Pan, X. Hao, G. Chen, B. Lü, J. Rao, F. Peng, Bio-based hot-melt adhesive from xylan, Nat. Sustain. 8 (2025) 827–836, https://doi.org/10.1038/s41893-025-01579-9.
[51] J. Xu, Y. Xia, Z. Li, H. Chen, X. Wang, Z. Sun, W. Yin, Multi-physics instrument: total scattering neutron time-of-flight diffractometer at China Spallation neutron source, Nucl. Instrum. Methods Phys. Res. Sect. A-Accel. Spectrom. Dect. Assoc. Equ 1013 (2021) 165642, https://doi.org/10.1016/j.nima.2021.165642.
[52] W. Zuo, A. Innocenti, M. Zarrabeitia, D. Bresser, Y. Yang, S. Passerini, Layered oxide cathodes for sodium-ion batteries: storage mechanism, electrochemistry, and techno-economics, Acc. Chem. Res. 56 (2023) 284–296, https://doi.org/10.1021/acs.accounts.2c00690.
[53] Z. Cui, C. Liu, A. Manthiram, A perspective on pathways toward commercial sodium-ion batteries, Adv. Mater. 37 (2025) 2420463, https://doi.org/10.1002/adma.202420463.
[54] A. Yao, S.M. Benson, W.C. Chueh, Critically assessing sodium-ion technology roadmaps and scenarios for techno-economic competitiveness against lithium-ion batteries, Nat. Energy 10 (2025) 404–416, https://doi.org/10.1038/s41560-024-01701-9.